Geophysical Journal International

Geophys. J. Int. (2010) **181,** 741–755 doi: 10.1111/j.1365-246X.2010.04544.x

A feasibility study of land CSEM reservoir monitoring in a complex 3-D model

M. Wirianto,[1] W. A. Mulder[1,2] and E. C. Slob[1]

[1] *Department of Geotechnology, Delft University of Technology, PO Box* 5048, 2600 *GA Delft, The Netherlands. E-mail: marwan_wirianto@yahoo.com*
[2] *Shell International E&P, PO Box* 60, 2280 *AB Rijswijk, The Netherlands*

Accepted 2010 January 26. Received 2010 January 26; in original form 2009 January 16

SUMMARY

We carried out a series of numerical simulations in a complex 3-D resistivity model to investigate the feasibility of using controlled-source electromagnetics on land for monitoring changes in a hydrocarbon reservoir during production. Displacement of oil by saline water injection changes the resistivity. The modelling allows a comparison of the measured time-lapse EM signal to various sources of noise that can be expected in a field experiment, for instance, magnetotelluric signals, repeatability errors and near-surface resistivity changes caused by seasonal variations. Our estimates show that land CSEM monitoring should be feasible, though not easily, for the example considered here, a thick reservoir at a depth of about 1 km. The trade-off between signal strength and repeatability errors requires the source to be located at some distance from the reservoir. Measurements in a monitoring well suffer less from surface noise. Measuring the vertical electric component in a well, placed at some distance from the reservoir, provides the best result.

Key words: Numerical approximations and analysis; Downhole methods; Electrical properties.

1 INTRODUCTION

The controlled-source electromagnetic (CSEM) method for hydrocarbon exploration was introduced in the 1980s by the Scripps Institution of Oceanography (Cox 1981; Cox *et al.* 1986; Evans *et al.* 1991), the University of Toronto (Cheesman *et al.* 1987) and Cambridge University (Evans *et al.* 1991). Commercial acceptance was reached much later (Eidesmo *et al.* 2002; Ellinsgrud *et al.* 2002). Since then, the marine CSEM method received more and more attention from the oil and gas industry. CSEM surveys on land have a longer history and have been carried out in, for instance, Russia, China and India (He *et al.* 2007; Strack & Pandey 2007). In some cases, CSEM measurements were used as the only exploration tool. In other, it complemented seismic surveys by providing an indication of the resistivity of targets identified by seismic imaging (Eidesmo *et al.* 2002; Darnet *et al.* 2007; MacGregor *et al.* 2007). This information can improve the probability of success in hydrocarbon exploration. Marine CSEM measurements are mostly processed in the frequency domain, whereas for land applications, both the time domain and the frequency domain are used.

A potential application of controlled-source EM is monitoring a hydrocarbon reservoir during the recovery process. Oil production with water flooding or steam injection, for instance, creates resistivity changes in the subsurface. These changes occur primarily in the reservoir. Smaller effects may be caused by changes in the near surface. A central question in EM monitoring is whether or not resistivity changes in the reservoir are detectable, and if so, if the value of that information is worth the effort compared to more established methods as time-lapse seismic measurements (Landrø *et al.* 2003; Vasco *et al.* 2008) that provide far better resolution, but not necessarily of the same quantity. In the EM case, spatial resolution will always be poor due to the diffusive character of EM signals in the earth at the low frequencies required to reach sufficient depth (Ward & Hohmann 1987). However, EM measurements are more sensitive to fluid properties than seismic measurements, especially when comparing highly resistive oil to low-resistivity brine. Although it would be interesting to compare or combine the CSEM data with other geophysical data sets, we do not consider that here. Instead, we focus on the feasibility of CSEM reservoir monitoring.

Several authors have undertaken an assessment of the feasibility of CSEM monitoring, for example Lien & Mannseth (2008), Orange *et al.* (2009) and Black & Zhdanov (2009). They all presented a modelling study of the CSEM monitoring problem for marine applications. Lien & Mannseth (2008) and Black & Zhdanov (2009) employed a 3-D integral-equation method to model the time-lapse effect of the flooding front during water injection into an oil reservoir. Orange *et al.* (2009) used an accurate 2-D finite-element modelling code to study several scenarios for depleting a reservoir, including lateral and bottom flooding, stacked reservoirs, and partial depletion. Here, we use a 3-D finite-volume code to study oil displacement by a water drive in a complex 3-D resistivity model and to assess if time-lapse changes are detectable with the land CSEM method.

From a practical point of view, monitoring the reservoir onshore is much easier than offshore, although the noise influence on EM data could be much stronger compared to the marine case. Also,

the accessibility of certain land areas may be restricted. In a marine environment with EM detectors on the sea bottom, the presence of several hundreds of metres of salt water will shield magnetotelluric and man-made EM signals, at least at higher frequencies. Also, source and receiver coupling are less of an issue. On the other hand, sea water currents create electric disturbances that increase the amount of background noise. On land, source and receiver coupling is a problem, as are natural and cultural sources of EM 'noise'. Land measurements are also susceptible to near-surface effects due to seasonal and diurnal changes, weather conditions such as rainfall and frost, and variations in ground water level. Both on land and in the sea, instrument noise and dynamic range play a role. Differences in positioning and variations in instrument properties cause repeatability errors. Still, a relative accuracy of the order of one percent should be feasible with careful and extensive calibration and pre-processing.

In this paper, we present a modelling study with the aim to investigate the potential use of land electromagnetic measurements for reservoir monitoring. We selected a reasonably complex geological model. In that model, we conducted numerical experiments to study the sensitivity of EM data to changes in an oil-bearing reservoir due to water injection. We assume that the CSEM measurements are available in the frequency domain. We considered measurements with sources and receivers at the surface as well as an acquisition geometry with sources at the surface and receivers in a monitoring well. We included noise and repeatability errors to assess the feasibility of land CSEM reservoir monitoring.

The outline of the paper is as follows. We first review the governing equations in the frequency domain, their discretization, and the solution method. Next, we describe the 3-D model with the oil reservoir. We then investigate various aspects of CSEM monitoring, such as the choice of frequency and the effect of the position of the source on the time-lapse data. After examining the surface-to-surface case, we consider sources at the surface and receivers in a monitoring well. The effect of various kinds of noise, both additive and multiplicative, is studied in Section 6 and affects the choice of acquisition geometry.

2 METHOD

In this section, we review the governing equations, their finite-volume discretization, and the numerical solution method. The electromagnetic wavefields are the electric field, $\hat{\mathbf{E}}(\mathbf{x}, t)$, and the magnetic field, $\hat{\mathbf{H}}(\mathbf{x}, t)$. Here $\mathbf{x} = (x_1, x_2, x_3)$ denotes the Cartesian coordinate vector and t is time. As usual, the x_3-axis is pointing downward. We define the temporal Fourier transform of a space- and time-dependent vector field $\mathbf{E}(\mathbf{x}, t)$ as

$$\mathbf{E}(\mathbf{x}, \omega) = \int_{-\infty}^{\infty} \hat{\mathbf{E}}(\mathbf{x}, t) \mathrm{e}^{\mathrm{i}\omega t}\, \mathrm{d}t, \tag{1}$$

where i is the imaginary unit and ω the angular frequency. The behaviour of electric field in conducting media can be described by Maxwell's equations and Ohm's law (*cf*. Ward & Hohmann 1987; Griffiths 1999; Jackson 1999). In the frequency domain at an angular frequency ω, these can be combined into

$$\mathrm{i}\omega\mu_0\tilde{\sigma}\mathbf{E} - \nabla \times \mu_r^{-1} \nabla \times \mathbf{E} = -\mathrm{i}\omega\mu_0 \mathbf{J}_s, \tag{2}$$

where $\mathbf{J}_s(\mathbf{x}, \omega)$ denotes the current source. The parameters $\tilde{\sigma}(\mathbf{x}) = \sigma - \mathrm{i}\omega\epsilon_0\epsilon_r$, with $\sigma(\mathbf{x})$ the conductivity, $\epsilon_r(\mathbf{x})$ the relative permittivity, $\mu_r(\mathbf{x})$ the relative permeability and ϵ_0 and μ_0 their absolute values in vacuum. The magnetic field, $\mathbf{H}$, follows from the relation

$$\nabla \times \mathbf{E}(\mathbf{x}, \omega) = -\mathrm{i}\omega\mu_r\mu_0 \mathbf{H}(\mathbf{x}, \omega). \tag{3}$$

To compute a numerical solution of eq. (2) for a given conductivity and source term, we discretized the equations on a tensor-product Cartesian grid allowing for grid stretching. Here, we employed the Finite Integration Technique (Weiland 1977), which can be considered as a finite-volume generalization of the scheme by Yee (1966). The discretization starts with a grid of block-shaped cells. The three electric field components are represented as average value on edges, the x-component on edges parallel to the x-direction and likewise the y- and z-component parallel to their corresponding directions.

Perfectly electric conducting (PEC) boundary conditions, namely $\mathbf{E} \times \mathbf{n} = 0$ with $\mathbf{n}$ the normal to the boundary, are used where the model is truncated. To avoid undesirable boundary effects, we added a boundary strip of about five skin depths around the model. For the air layer, an even thicker layer is added. Grid stretching is necessary to balance the need for an accurate solution around the area of interest and the limitations of available computer memory. Several conflicting requirements guide the choice of the grid. We refer to the paper by Plessix *et al.* (2007) for more details.

Discretization of the system of eq. (2) together with the PEC boundary conditions leads to a linear system of the form

$$\mathbf{L}^h \mathbf{E}^h = \mathbf{f}^h,$$

where $\mathbf{L}^h$ is the discrete Maxwell operator, $\mathbf{E}^h$ the vector of the discrete values of the electric field and $\mathbf{f}^h$ the source vector. The matrix $\mathbf{L}^h$ is large, symmetric but not Hermitian, and sparse. We solved the discrete equations with an iterative method, BiCGSTAB2 (van der Vorst 1992; Gutknecht 1993), preconditioned by a multigrid solver (Mulder 2006). The method is matrix-free: we never explicitly form the large sparse linear matrix that describes the discretized problem but only evaluate its action on the latest estimate of the solution, thereby reducing storage requirements. For applications of this solver, we refer to Mulder (2006), Plessix *et al.* (2007) and Mulder *et al.* (2008).

In addition, we applied the well-known primary-secondary field formulation, described here for completeness. In this formulation, the electrical field $\mathbf{E}$ is expressed as the sum of a primary and secondary component. The primary field is obtained for a background model and should be easy to compute, whereas the secondary field can be computed as follows. Eq. (2) in operator notation reads

$$\mathbf{L}_\sigma \mathbf{E} = \mathbf{f}, \tag{4}$$

where $\mathbf{L}_\sigma = \mathrm{i}\omega\mu_0\tilde{\sigma} - \nabla \times \mu_r^{-1} \nabla \times$, and $\mathbf{f} = -\mathrm{i}\omega\mu_0 \mathbf{J}_s$. Suppose we have a background model σ_b and electric field $\mathbf{E}_b$ that satisfies

$$\mathbf{L}_{\sigma_b} \mathbf{E}_b = \mathbf{f}. \tag{5}$$

By letting $\mathbf{E} = \mathbf{E}_b + \mathbf{E}_s$ where $\mathbf{E}_s$ is the secondary solution that we want to compute, Eq. (4) can be rewritten as

$$\mathbf{L}_\sigma \mathbf{E}_b + \mathbf{L}_\sigma \mathbf{E}_s = \mathbf{f}. \tag{6}$$

This separation can be performed because the operator $\mathbf{L}_\sigma$ is linear with respect to the field $\mathbf{E}$. Since the operator $\mathbf{L}$ is also linear with respect to the model parameter σ, the first term on the left-hand side can be expressed as $\mathbf{L}_\sigma \mathbf{E}_b = \mathbf{L}_{\sigma_b} \mathbf{E}_b + \mathbf{L}_{\sigma_s} \mathbf{E}_b$, where $\sigma_s = \sigma - \sigma_b$. Then, by substituting eq. (5) into eq. (6), we obtain the system of equations for the secondary solution,

$$\mathbf{L}_\sigma \mathbf{E}_s = -\mathbf{L}_{\sigma_s} \mathbf{E}_b.$$

The secondary system of equations is the same as the original one except for the source term.

The primary-secondary field formulation does not change the convergence speed of the iterative method, but may provide more accurate results, for instance, when the source resembles a delta

function. In that case, the solution will be singular close to the source and a rather fine grid will be required to resolve the singular behaviour of the electric field. The primary-secondary formulation allows for an analytical treatment of the source singularity and, therefore, does not require very small cells close to the source point. We used the exact solution for a homogeneous half space (Raiche & Coggon 1975) with a resistivity equal to that at the source location as the primary field.

3 BASE MODEL

As a starting point for studying the monitoring problem, we modified the SEG/EAGE Overthrust model (Aminzadeh *et al.* 1997) to obtain a realistic and complex subsurface resistivity, replacing velocities by resistivities according to $\rho = (v/1700)^{3.88}$, as suggested by Meju *et al.* (2003). Here, v is the velocity in metres per second and ρ the resistivity in Ohm metre. The model has a size of 20 km $\times$ 20 km $\times$ 4.7 km.

In the 3-D model, we selected one part as an artificial reservoir sand that contains oil and water. We then defined two different states, the initial condition of the reservoir and a later state where part of the oil has been replaced by water. For simplicity, we assumed that the recovery process only affects the configuration of oil and water in the reservoir, so that the differences in the time-lapse data are entirely due to changes in this part. We start with this idealized situation and will make modifications later on.

Fig. 1 shows a vertical slice through the model at $y = 3000$ m for two different states, the initial condition of the reservoir and a later state where the oil–water contact has risen 100 m after water injection. We will start with the assumption of 100 per cent sweep efficiency, meaning perfect replacement of oil by water. Archie's law (Archie 1942) relates the *in situ* resistivity of sedimentary rock to its porosity and water saturation by

$$\rho_t = \rho_w \phi^{-m} S_w^{-n},$$

where ϕ denotes the porosity, ρ_t the resistivity of the fluid saturated rock, ρ_w represents the resistivity of the water, and S_w the water saturation. The constants m and n are the cementation and saturation exponents, respectively. Archie (1942) found that m is approximately 1.8–2.0 for consolidated sandstones and 1.3 for clean, unconsolidated sands. He also determined that the saturation exponent is approximately 2.0. If we use 2.0 for both constants m and n and assume that the saturated rock has a porosity of 40 per cent and a water saturation of 100 per cent, we obtain a resistivity of about 2 Ohm m, given a resistivity of 0.33 Ohm m for the salt water injected during the recovery process. The resistivity in the oil-bearing part of the reservoir sand is set to 100 Ohm m.

We added extra boundary strips of about five skin depths in the x- and y-directions and at the bottom of the model to avoid undesirable boundary effects. The skin depth at a frequency f is $1/\sqrt{\pi f \sigma \mu}$, where σ is the conductivity and μ the permeability. In our case, σ is set to 0.5 S/m and μ is set to its vacuum value, $\mu_0 = 4\pi 10^{-7}$ H/m. On the top of the model, we added an air layer with resistivity value of 10^{11} Ohm m and a thickness of about 40 km. We defined a computational grid with 128 by 128 by 128 cells, leading to over 2 million grid points with about 6 million unknowns. The cell widths of the stretched grid varied from 25 m to about 5 km. A finer grid would increase the computational time. Later on, we will assess the numerical accuracy by comparing results for 128^3 and 256^3 grid cells.

4 SURFACE-TO-SURFACE EM

We consider time-lapse EM effects due to resistivity changes during reservoir depletion with a water drive. We assume simple bottom depletion in which the oil–water contact has moved up 100 m as would happen as a result of water injection in the deeper parts of the reservoir by means of a horizontal well. We start with the assumption of 100 per cent sweep efficiency. Although this assumption is overoptimistic, the difference between 100 per cent and more reasonable sweep efficiency will not be too dramatic. This is because the resistivity contrast between mixture-saturated part and oil-bearing is still high. If, for example, the sweep efficiency is 40 per cent, Archie's law predicts a resistivity around 10 Ohm m for the rock that contains the oil–water mixture. This is still a small number compared to the resistivity of the oil-bearing part. Later on, we will show a comparison between 100 and 40 per cent sweep efficiency.

We first determine the frequency that is most sensitive to the change in the reservoir. We measured the time-lapse change in a surface-to-surface configuration, placing both the source and the receivers on the surface. A unit dipole source in the x-direction is positioned at (2000, 11 375, 0) m. We placed a receiver at (7000, 11 375, 0) m and then computed the in-line electric field E_1. Fig. 2 shows the in-line electric field components as a function of frequency. We observe the largest relative difference between 1 and 2 Hz, whereas the difference rapidly decreases above 2 Hz. The relative differences for frequencies above 5 Hz are smaller than 1 per cent because of the strong attenuation of high-frequency electromagnetic waves in the earth.

Fig. 3 displays the amplitude behaviour of time-lapse difference for the in-line electric field measured on the surface. We still assume idealized conditions, that is, the difference is entirely due the resistivity change in the reservoir. The time-lapse resistivity changes are examined by considering the amplitudes of the absolute as well as the normalized differences of the electric field. Measuring the absolute differences is useful to identify domains with signal changes above the noise floor, which is independent of the signal strength, while measuring the normalized differences is useful to identify domains with signal changes that lie above a noise level and are proportional to the signal strength, such as the repeatability errors. The results in top panels of Fig. 3 show the effect of frequency on the absolute amplitude of the difference. The high frequency on the left provides a far better resolution than the lower frequencies to the right. The plots in bottom panels of Fig. 3 display the relative change $|\Delta E_1|/\sqrt{|E_1|^2 + |E_2|^2}$ on a logarithmic scale. We impose a lower bound of 1 per cent for the multiplicative noise, because we assume that repeatability errors only allow for reliable measurements of relative differences above 1 per cent. We observe that the resistivity change at 10 Hz can hardly be detected, but that we have a clear effect above the reservoir at 1 and 0.1 Hz. Fig. 3 shows that at 10 Hz, the time-lapse change is more spatially confined to the reservoir region but that their amplitude is too small to be detectable because the attenuation is too strong at this high frequency.

As already stated, we used a computational grid with 128 $\times$ 128 $\times$ 128 cells, with cell widths varying from 25 m to about 5 km. Convergence, with a relative drop in the residual of 10^{-7}, took about 30 minutes using a 2.2-GHz AMD Opteron with 16 GB of memory. We oversampled the result on a very fine grid using standard trilinear interpolation. To check if the result is accurate enough, we ran the same simulation but now with a finer grid of 256 $\times$ 256 $\times$ 256 cells. The number of iterations to reach convergence remained the same. Fig. 4 displays the amplitude behaviour of the in-line electric field with the initial model at 1 Hz using two computational

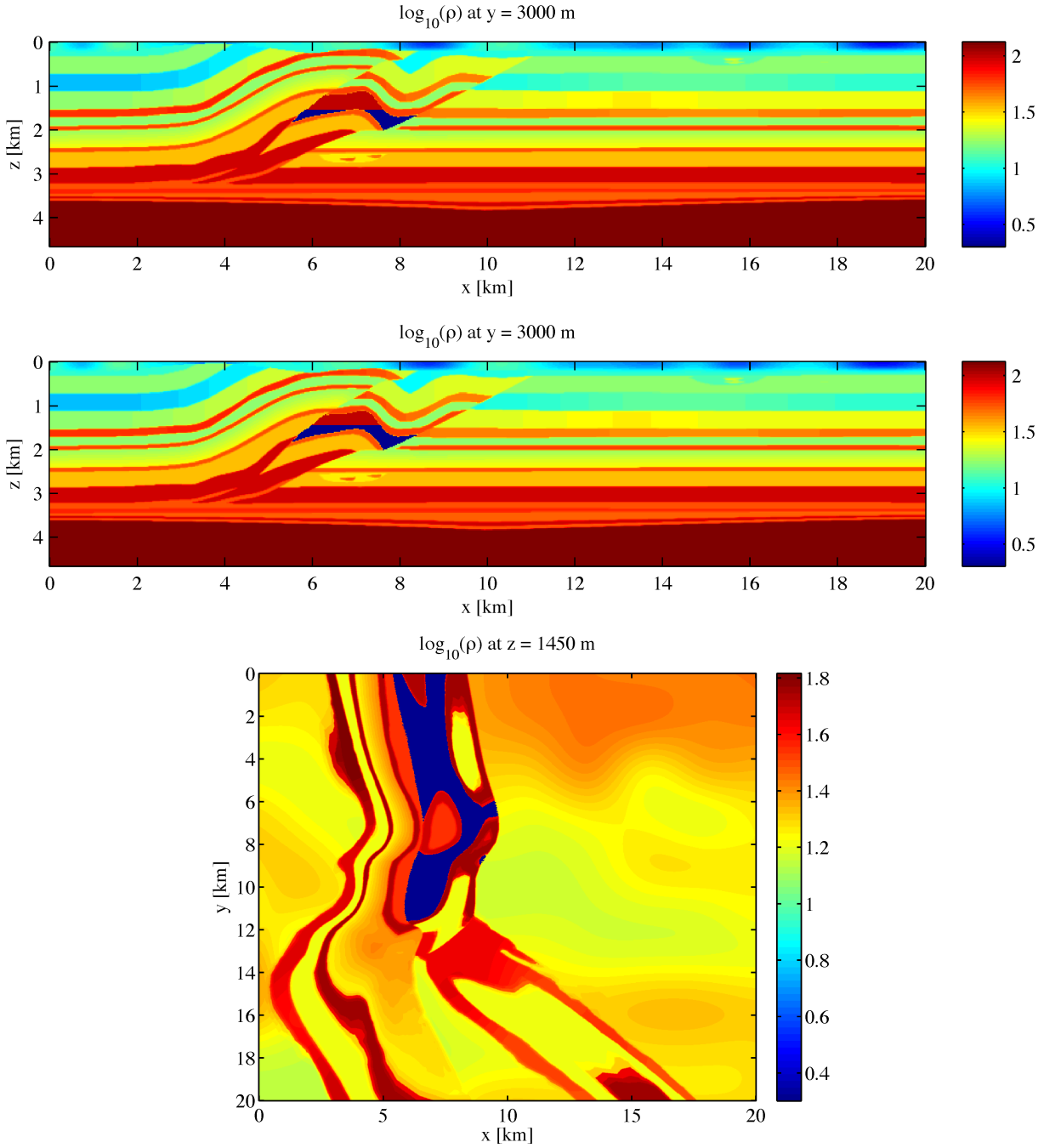

Figure 1. Resistivity based on the SEG/EAGE Overthrust model. The reservoir formation lies around $x = 6$ km and between 1.4 and 2.0 km depth in this section of the model. The dark blue part shows the injected water. The oil-bearing sand above it is coloured dark red. In the middle panel, the oil–water contact has moved up 100 m relative to top panel. The bottom panel shows a horizontal cross-section of the middle panel at 1450 m depth.

grids. We observe that the responses display the same qualitative behaviour either with 128^3 or with 256^3 cells. There are certainly differences between those two results as indicated by the dashed line in Fig. 4, but the values are relatively small and seem to be below 1 per cent. This is smaller than the assumed size of the repeatability errors. Fig. 5 displays the amplitude behaviour of time-lapse difference at 1 Hz using the two computational grids. Again, we observe that the results display the same qualitative behaviour for the result obtained with 128^3 or with 256^3 cells. Small differences can be observed in the absolute time-lapse variations, displayed in the two top panels of Fig. 5, but the numerical errors are less obvious in the normalized time-lapse differences shown at the bottom. We conclude that it is sufficient for our purpose to use the computational grid with 128^3 cells. We refer to Mulder (2006, 2008) and Mulder *et al.* (2008) for more details about the performance of the method.

So far, we considered only a source positioned at (2000, 11 375, 0) m. This source location may not be optimal. We ran the same experiment but now with different source positions along a line in the x-direction. We still considered the surface-to-surface configuration. The frequency was fixed at 1 Hz and the computational grid had 128^3 cells.

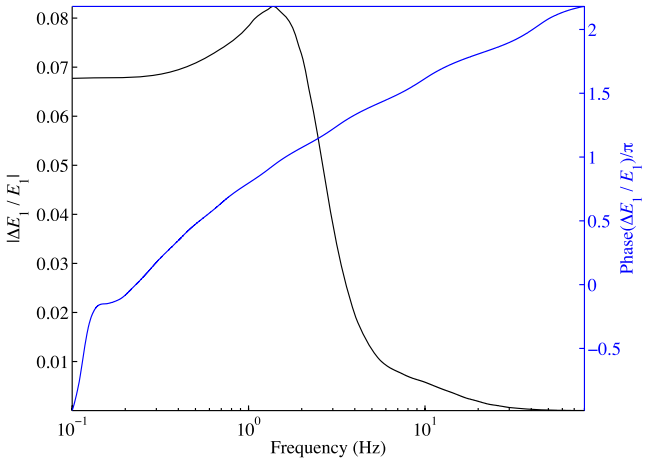

Figure 2. Relative difference of the electric field components in x-direction, E_1, for a receiver at (7000, 11 375, 0) m or 5 km distance from the source. Both the amplitude and the normalized unwrapped phase angle (the unit is π or 180°) are shown.

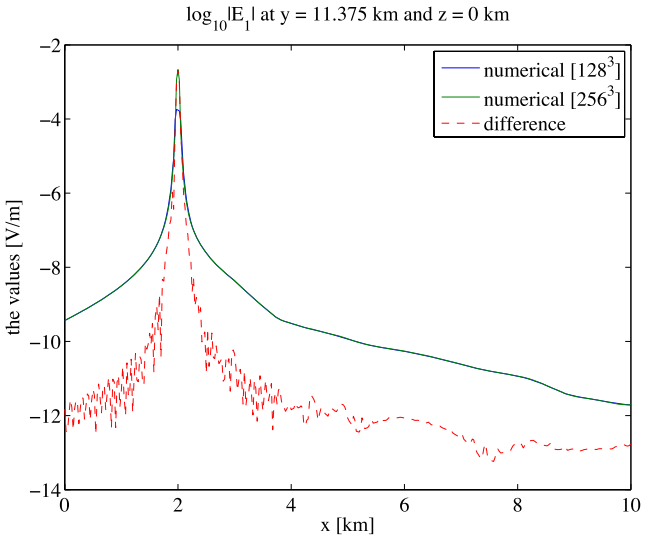

Figure 4. The amplitude behaviour of the electric field components in x-direction, E_1, for a receiver array at $(y, z) = (11\,375, 0)$ m. The legend with 'numerical [128^3]' means the result computed with 128^3 cells, while 'numerical [256^3]' is with 256^3 cells.

Fig. 6 displays the effect on the absolute and relative change. Here we only show the results for three source positions, namely (4000, 11 375, 0) m, (8000, 11 375, 0) m, and (14 000, 11 375, 0) m. The top-centre panel of Fig. 6 suggest that the source at $x = 8000$ m provides higher sensitivity. We observe that the absolute amplitude of the difference is higher than the result with the source at $x = 4000$ m or $x = 14\,000$ m. However, we lose the time-lapse effect when we consider the relative change. The relative amplitudes in an area of about 2 km around the source location have become too small, as shown in the bottom-centre panel of Fig. 6. This is caused by the fact that the near-field signals are dominated by the direct field. Repeatability errors in the strong field around the source will exceed the signal difference due to the resistivity changes in the reservoir. We obtain a better result for the source at $x = 14\,000$ m, where the time-lapse variation, both in terms of the amplitude difference as well as in relative change, is spatially better confined to the reservoir region. These results suggest that we should place the source not too close to the target area. We repeated the experiment for sources along a line in the y-direction. The y position is now fixed at 14 000 m. The top panels of Fig. 7 display the effect on

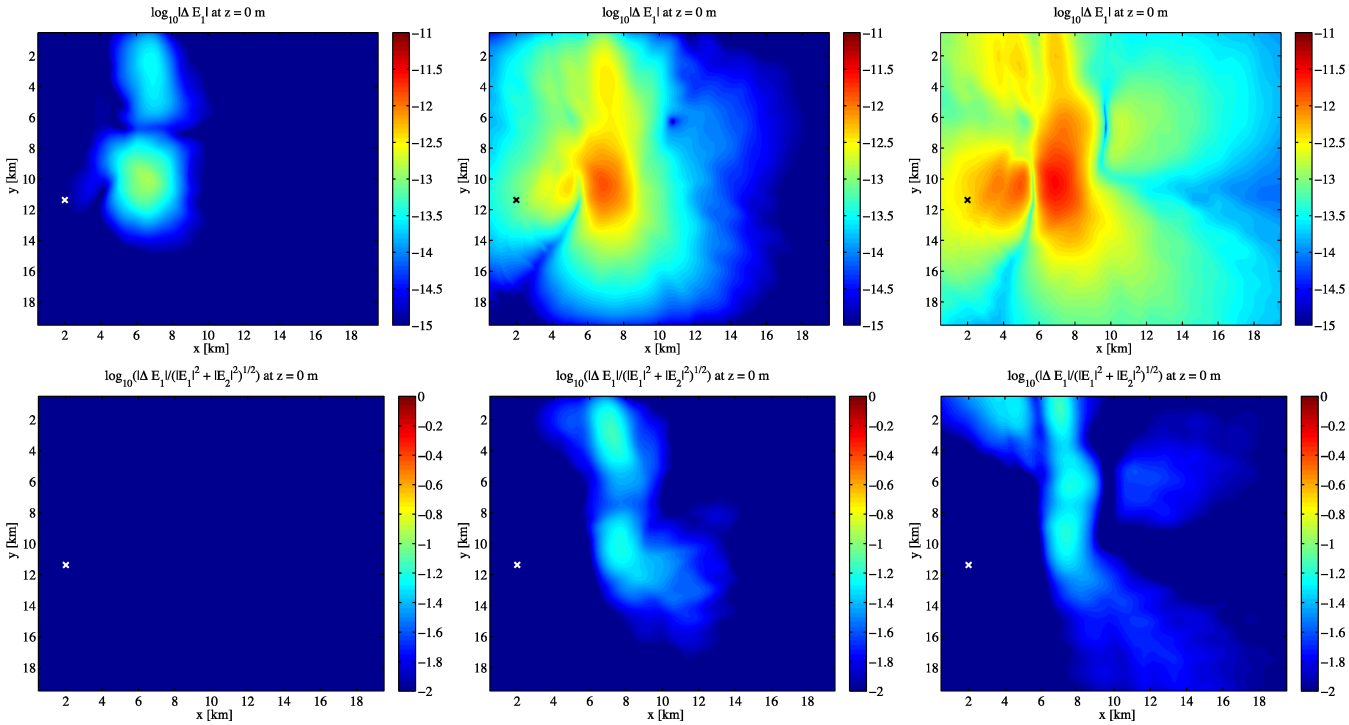

Figure 3. The top panels display the time-lapse differences of the in-line electric field observed on the surface (top view) at frequencies of 10, 1 and 0.1 Hz, from left- to right-hand panels. The bottom panels display the normalized fields with amplitudes below 1 per cent suppressed, as these are assumed to be dominated by noise.

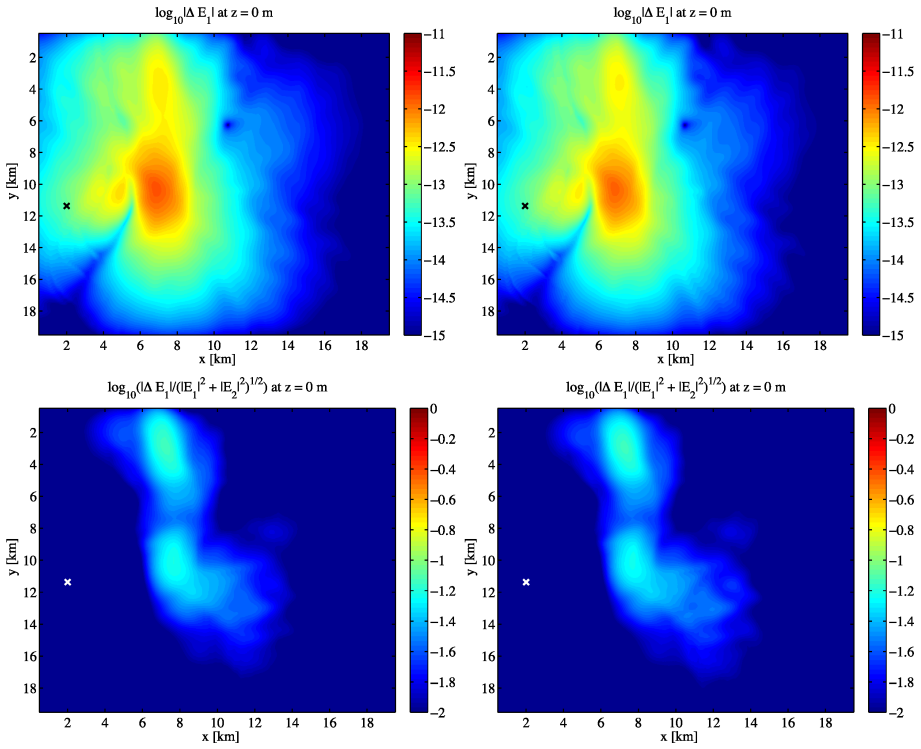

Figure 5. The top panels display the time-lapse differences of the in-line electric field observed on the surface (top view) at 1 Hz with the computational grid of 128^3 and 256^3 cells, from left- to right-hand panels. The bottom panels display the normalized fields with amplitudes below 1 per cent suppressed.

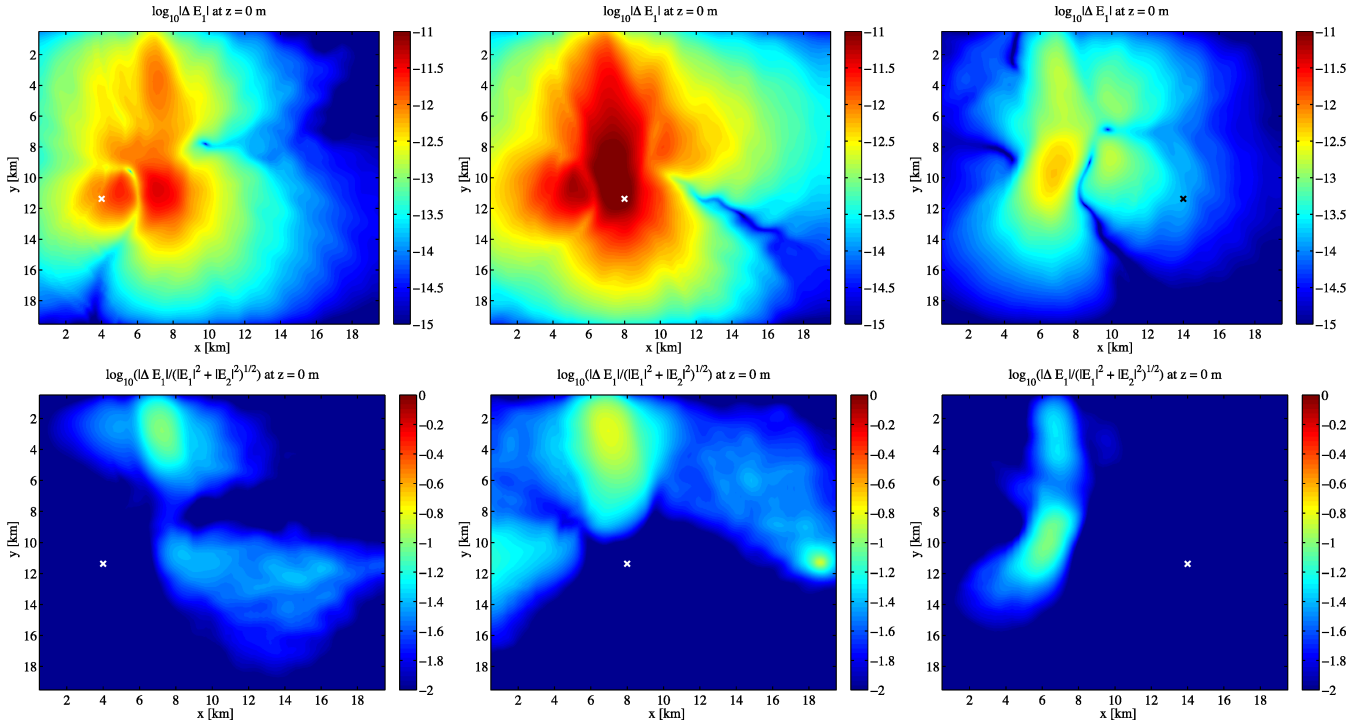

Figure 6. The top panels show the time-lapse differences of the in-line electric field at 1 Hz, observed on the surface (top view) with source positions at $x =$ 4, 8, and 14 km, from left- to right-hand panels. The y and z source coordinate is the same as in the first experiment. The bottom panels display the normalized fields with amplitudes below 1 per cent removed.

the absolute amplitude change at $x = 4000$, 8000 and 14 000 m, respectively, whereas the bottom panels show the relative change.

These results confirm that there are optimal distances between source, receivers and target area. If the source is close to the receiver and the target, the signal will be dominated by the direct field. Note that we will use the term 'direct field' to denote the electric field generated in the absence of a time-lapse change. The change in reservoir properties can be considered, to first order, as a

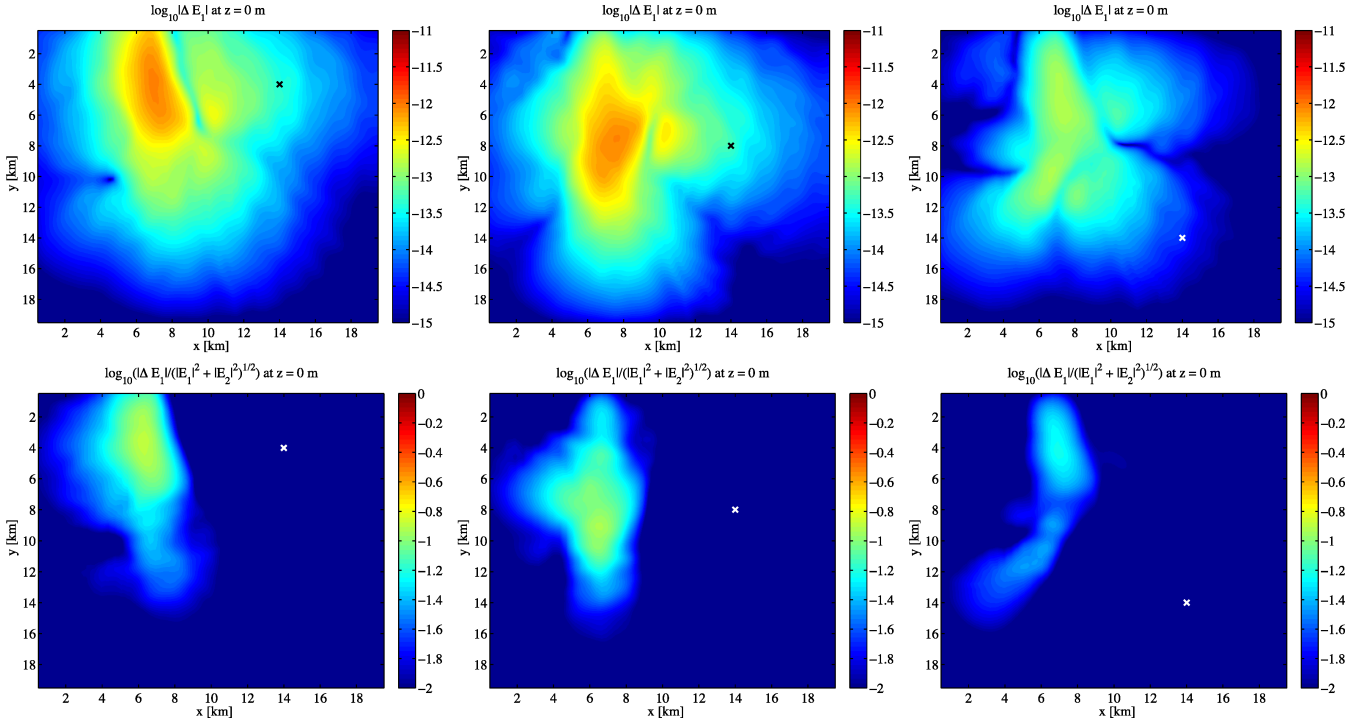

Figure 7. The top panels show the time-lapse differences of the in-line electric field observed on the surface (top view) with source positions at $y = 4$, 8 and 14 km, from left- to right-hand panels. The x-position is set to 14 km and z-position is at the surface. The bottom panels display the normalized fields with amplitudes below 1 per cent suppressed.

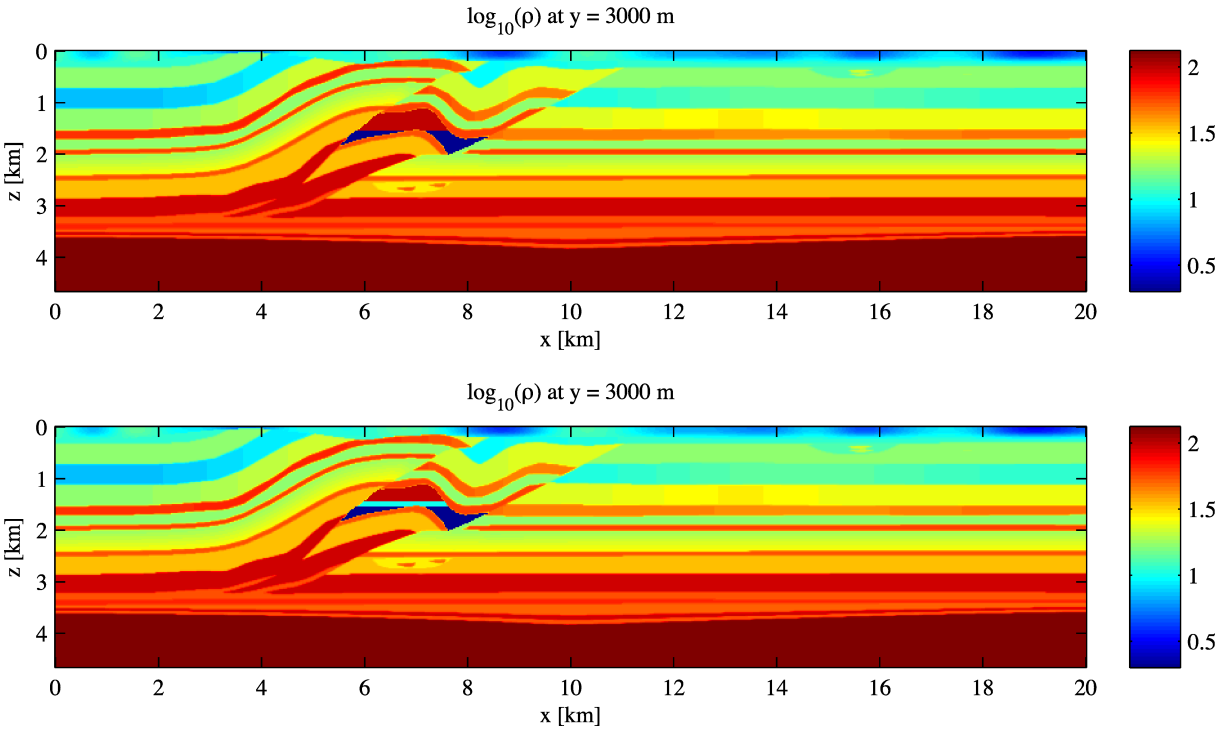

Figure 8. The light blue part in the bottom panel shows the part where the oil was partly replaced by water, having a 40 per cent water saturation. The top panel shows the initial condition.

scatterer that produces an additional signal. At large distances from the source, the signal of the time-lapse change is becoming too weak. Acquisition optimization, which we have not undertaken, should take these observations into account.

In the previous experiments, we have assumed a 100 per cent sweep efficiency. This choice may be overoptimistic. We repeated the experiments for a sweep efficiency around 40 per cent, assuming that not all the oil is replaced by water. The resistivity of the swept

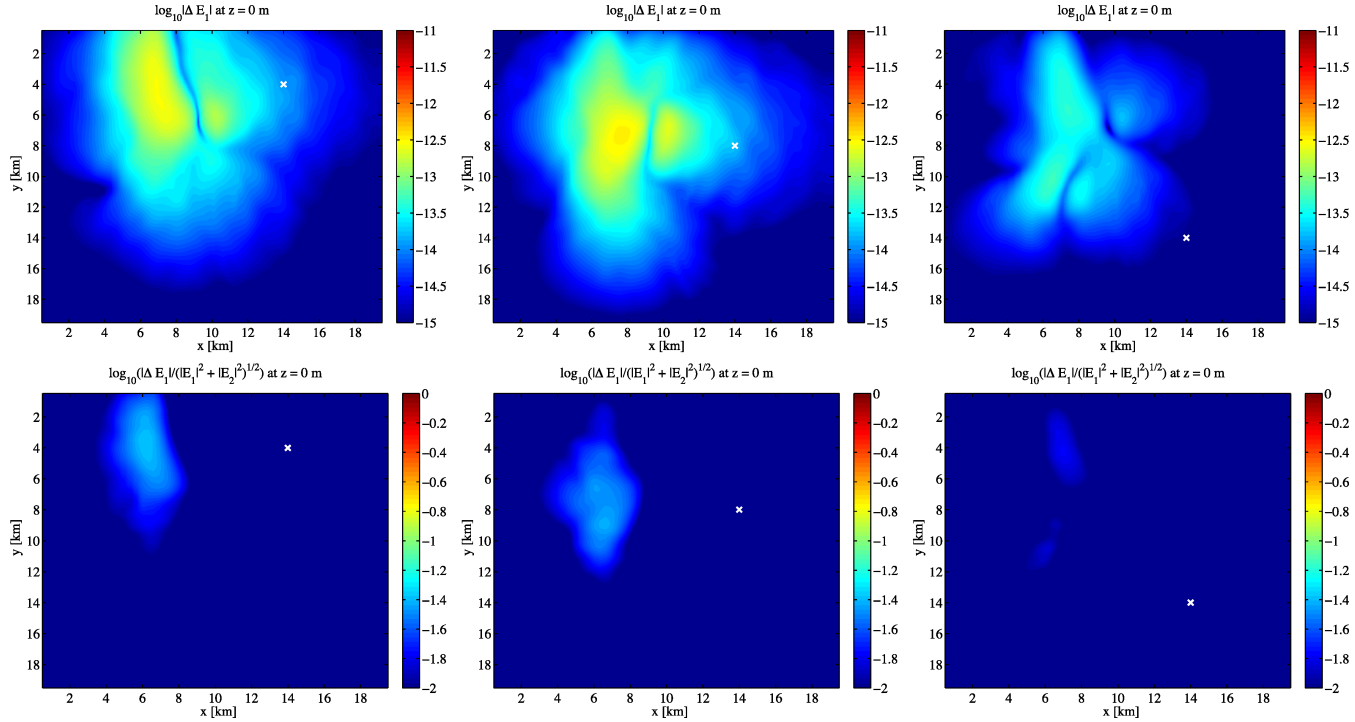

Figure 9. Absolute (top row) and relative (bottom row) time-lapse changes in E_1 for three different source positions marked by a cross, similar to Fig. 7, but for a sweep efficiency of 40 per cent.

oil is now set to 10 Ohm m instead of 2 Ohm m as in the case of 100 per cent sweep efficiency. Fig. 8 shows a vertical slice through the model at $y = 3000$ m before and after water injection. Fig. 9 displays the effect on the absolute and the relative change in the surface electric field for the same case as in Fig. 7, but now with the 40 per cent sweep efficiency applied. The difference between 100 and 40 per cent sweep efficiency is not too dramatic in terms of the overall shape of the time-lapse difference, but the absolute and relative amplitudes become smaller, as expected.

5 MONITORING WELL

So far, we considered only the surface-to-surface configuration, placing both the sources and the receivers on the surface. This configuration is the most obvious one to use on land, but may suffer from resistivity changes in the near-surface environment, as will be considered in Section 6. We therefore investigated another type of configuration, similar to vertical seismic profiling (VSP), namely surface-to-borehole measurements with sources on the surface and receivers in a monitoring well. We ran a number of experiments to study the feasibility of reservoir monitoring with this acquisition geometry.

In a typical vertical borehole EM survey, logging tools are usually fitted with sensors that consist of a magnetic channel and a vertical electric channel measuring E_3. The antenna for the horizontal electric channel will not fit. Nevertheless, we assume in our modelling study that all components can be recorded.

First, we looked for the component that is most sensitive to the reservoir change. We ran a simulation with the same configuration as in Fig. 6. A unit dipole source in the x-direction was positioned on the surface at (4000, 11 375, 0) m. We select this position, because the source should not be too close to and also not too far away from the target. Of course, the position may not be optimal, but

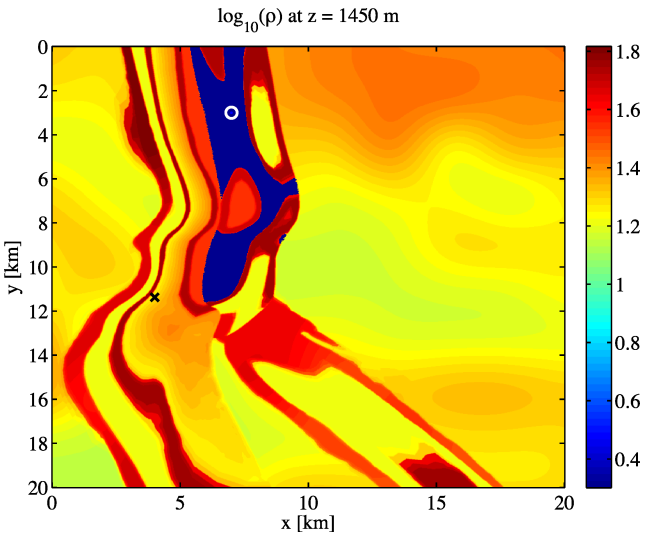

Figure 10. A horizontal cross-section of the resistivity at reservoir depth. The black cross marks the position of the source at $(x, y) = (4000, 11\,375)$ m. The white circle indicates the location of the vertical well at $(x, y) = (7000, 3000)$ m.

it is sufficient to start the investigation. The frequency was set to 1 Hz. The bottom-left panel of Fig. 6 shows that the strongest relative time-lapse change in E_1 occurs around $x = 7000$ m and $y = 3000$ m, so we placed the well at this position. The well location is marked by a circle in Fig. 10, displaying a horizontal cross-section of the resistivity at the reservoir level with the reservoir clearly visible in dark blue. The black cross indicates the surface source location.

Fig. 11 shows the response before and after water injection. The left-hand panel displays the resistivity log of the well. The

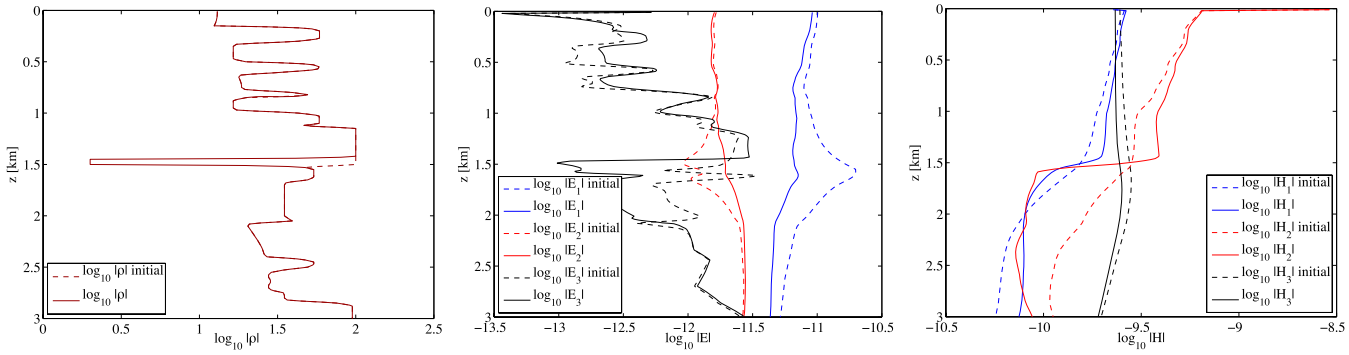

Figure 11. The left-hand panel displays the resistivity log in the well. The centre and the right-hand panel show, respectively, the electric and the magnetic field components for a dipole source in the x-direction at a frequency of 1 Hz. The dashed lines represent the initial fields, the drawn lines those after production.

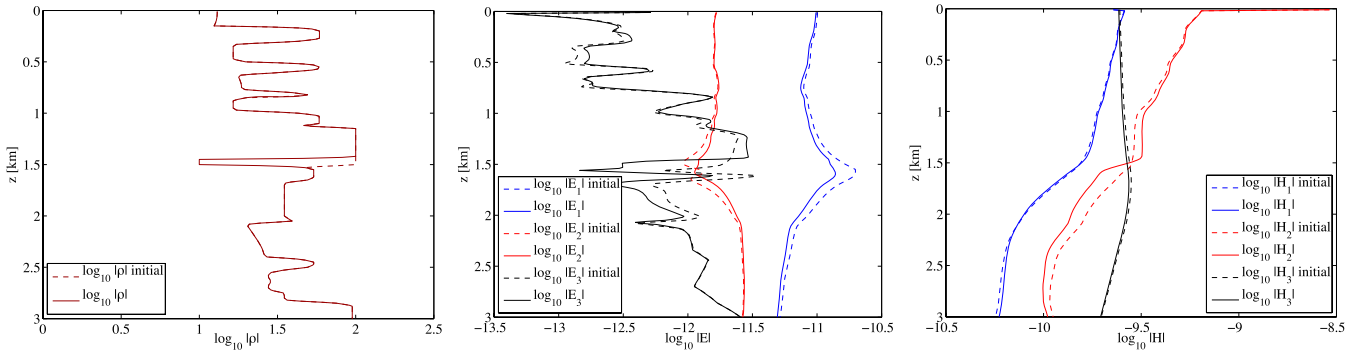

Figure 12. As Fig. 11, but assuming a sweep efficiency of 40 per cent.

reservoir is visible between depths from about 1 km to 1.5 km. The dashed lines represent the initial resistivities, the drawn lines the resistivities after production. The sweep efficiency is assumed to be 100 per cent. The centre and the right panels of Fig. 11 display the electric and the magnetic field components in the well. The dashed lines represent the initial fields, the solid lines show the fields after production. The effect of oil displacement is visible in all electric and magnetic components and the largest changes occur close to where the resistivity has changed. However, if we would consider a shallow well, Fig. 11 suggests that the vertical electric field component, E_3, captures the change best. This component is relatively easily measured in a vertical well. As in the surface-to-surface configuration, a lower sweep efficiency will generate a smaller time-lapse change in the measured signal as can be seen in Fig. 12, where we assumed a sweep efficiency of 40 per cent. Still, the effect of oil displacement is captured best by E_3. A small effect also appears in H_2, the magnetic field component in the y-direction. Note that the signature of E_3 on the bottom left-hand panel follows the resistivity log shown in the top right-hand panel.

Having established that measuring time-lapse changes of the vertical electric component, E_3, appears to be the best option for a monitoring well, the question remains what a good location for the well would be. To answer this question, we examined vertical cross-sections of the time-lapse differences in the electric field components for different source positions.Fig. 13 displays vertical cross-sections of the time-lapse differences in the three electric field components for a source in the x-direction at (4000, 11 375, 0) m, as in Fig. 11. We only show a single cross-section at $y = 3$ km. The left-hand panels display the absolute difference of E_1, E_2 and E_3, respectively, from top to bottom. The right-hand panels show the relative differences. We observe that the largest differences in E_1 and E_3 occur just below and above the reservoir. The differences for component E_1 extend all the way to the surface. This is a useful result, as the horizontal electric field components are easy to measure at the surface. For measurements in a well, the vertical component, E_3, captures the change best, as can be seen in the bottom right-hand panel of both Figs 11 and 13. We repeated the experiment for a different source positions on the surface, at (14 000, 4000, 0) m, the same position as in the left panels of Fig. 7 at some distance from the reservoir. The results are shown in Fig. 14. We can see a behaviour similar to what we can observe in Fig. 13.

At this point, it would seem that placing a vertical well through the reservoir appears to be a good way of capturing the change in the resistivity. With vertical, piston-like displacement, this a trivially true, but then a well-log would already be sufficient. If we want to monitor the reservoir as a whole, including lateral heterogeneities and variability in sweep efficiency due to variations in rock properties and faults, a single monitoring well in the reservoir may be less useful. In the experiments shown in Figs 13 and 14, the source was placed at some distance from the target. If, instead, we consider a source straight above the reservoir, a monitoring well in the reservoir is less useful as illustrated by Fig. 15. Here, we placed the source on the surface at (7500, 8000, 0) m, precisely above the reservoir. Fig. 15 displays a vertical cross-section at $y = 8$ km. We can see in the panels on the right-hand side that the relative time-lapse differences have become much smaller. This is due to the near-field signal being dominated by the direct field. Fig. 15 also shows that the relative change in the vertical component becomes larger for x larger than 14 km. This observation led us to consider a different type of acquisition.

Because the cost of drilling many wells is high, we want to look for an alternative, namely a walk-away survey, similar to a walk-away VSP in seismics, with a receiver in the well and sources placed at different positions on the surface. As we saw earlier that

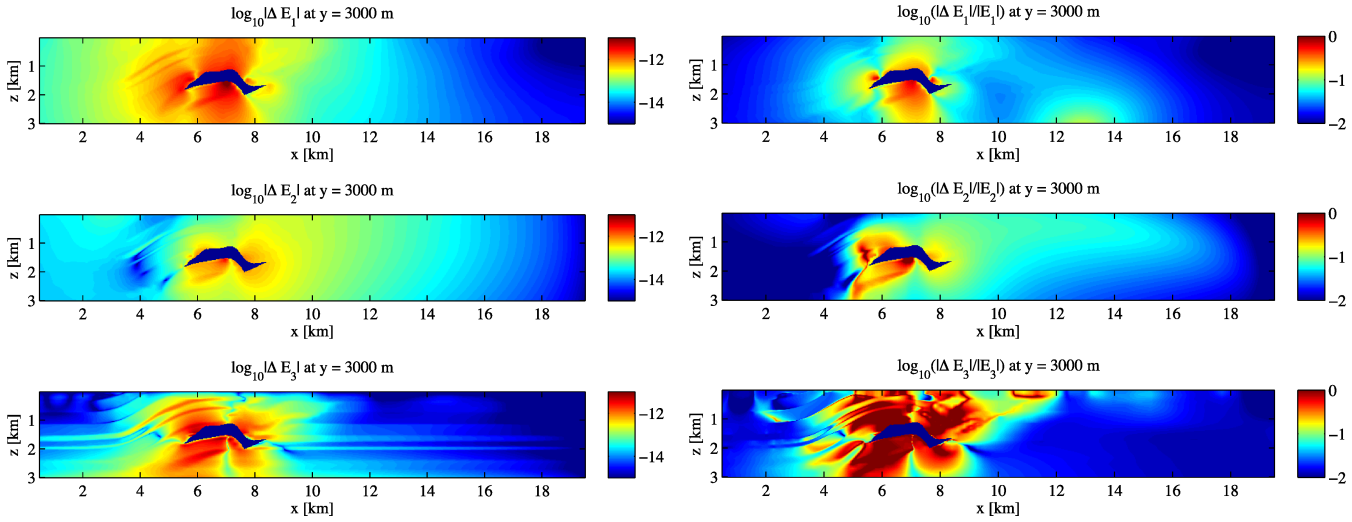

Figure 13. All panels display a vertical cross-section at $y = 3$ km with the same configuration as in Fig. 11. The left-hand panels display the absolute difference of E_1, E_2 and E_3, respectively, from top to bottom. The right-hand panels display the relative difference. The dark-blue area between $x = 6$ and 8 km coincides with the reservoir. The source was placed at (4, 11.375, 0) km, above the reservoir.

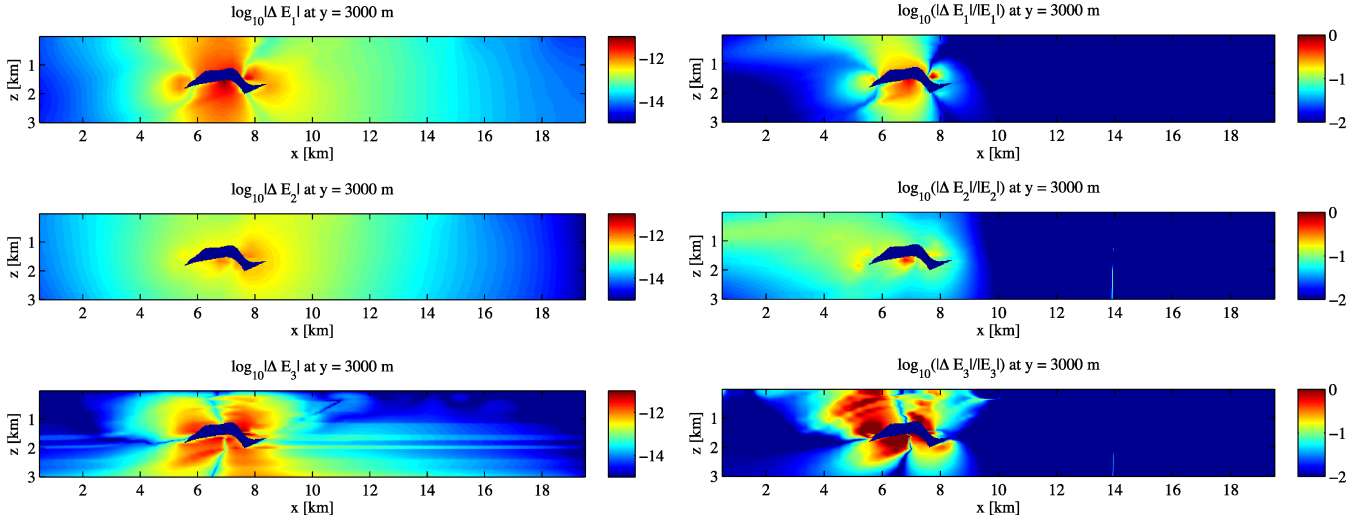

Figure 14. As Fig. 13, but for a source positioned at (14, 4, 0) km, as in the left-hand panel of Fig. 7.

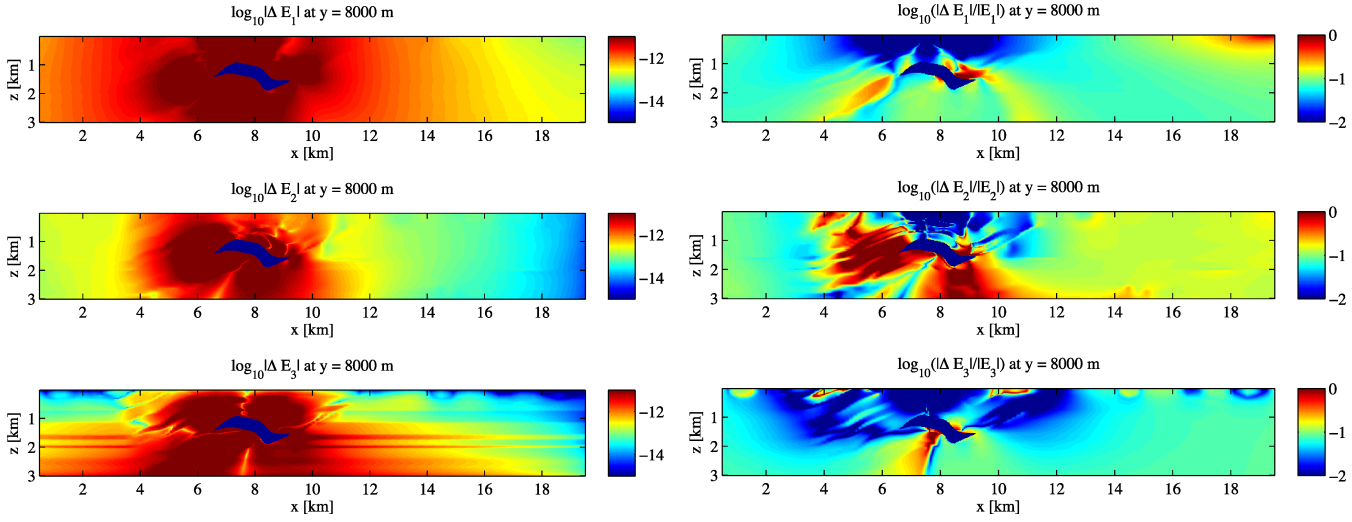

Figure 15. All panels display a vertical cross-section at $y = 8$ km of the time-lapse change in each of the three electric components for the same configuration as in Fig. 11, but with the source above the reservoir area at (7.5, 8, 0) km.

the vertical electric component was the most sensitive to changes in the reservoir, we concentrate on that component.

To avoid numerous computations for different sources at the surface, we used the source–receiver reciprocity theorem for the EM field (de Hoop 1995), interchanging the source and receiver positions. Instead of applying source current in the x-direction on the surface and measuring the vertical component E_3 in the well, we ran the experiment with a vertical-component current source in the well and measured E_1 on the surface. The results should be the same. We will use both points of view in the following discussion, but assume that sources are located on the surface and the receiver in the well for the actual experiment.

To study the walk-away configuration, we first placed a receiver in the well just above the reservoir at the position (6000, 2000, 900) m and measured the vertical electric component. The white circle in the left-hand panel of Fig. 16 shows the well location in map view. For the source positions, we simply took the entire surface of the model. The central panel of Fig. 16 displays the amplitude behaviour of the time-lapse difference for the vertical component, measured in the well for different source positions. We observe that the time-lapse change is spatially confined to the reservoir region, albeit with a low resolution. The strongest response appears when the source is placed close to the well. However, the picture changes completely when we consider the relative change, as shown in the right-hand panel of Fig. 16. The strong time-lapse signal in an area around the well location has disappeared. This effect is similar to what we found in the surface-to-surface configuration. If we take a closer look at the right-hand panel of Fig. 16, we observe that the larger relative differences occur at some distance from the well, as evidenced by the red to dark red colours. We conclude that the right-hand panel of Fig. 16 suggests a well location at some distance from the target. We repeated the experiment for a different well position at (14 000, 6000, 900) m. The results are shown in Fig. 17. We clearly obtain a better delineation of the change in the reservoir. The amplitude difference and the relative change are spatially better confined to the reservoir region.

If we use the same reasoning as for the surface-to-surface configuration, there should be an optimal distance between the well and the target area. If the source is close to the receiver and target, the signal will be dominated by the direct field. If the distance is too large, the signal is becoming too weak. We conclude that the walk-away configuration has a potential value for field experiments. Once a well has been drilled, this type of measurement is relatively easy to carry out with only one or a few receivers in the well and mobile source equipment.

6 NOISE ESTIMATES

So far, we have assumed that the time-lapse difference of the electric field is mainly due to oil being displaced by water. In field surveys, the measurements will always be affected by noise and limitations of the recording equipment. Obviously, equipment and measurement errors should be made as small as possible, but are impossible to avoid. In his book, Strack (1992) lists possible sources of errors that can show up in field CSEM surveys. Some of them are caused by the choice of hardware system, other by resistivity changes in

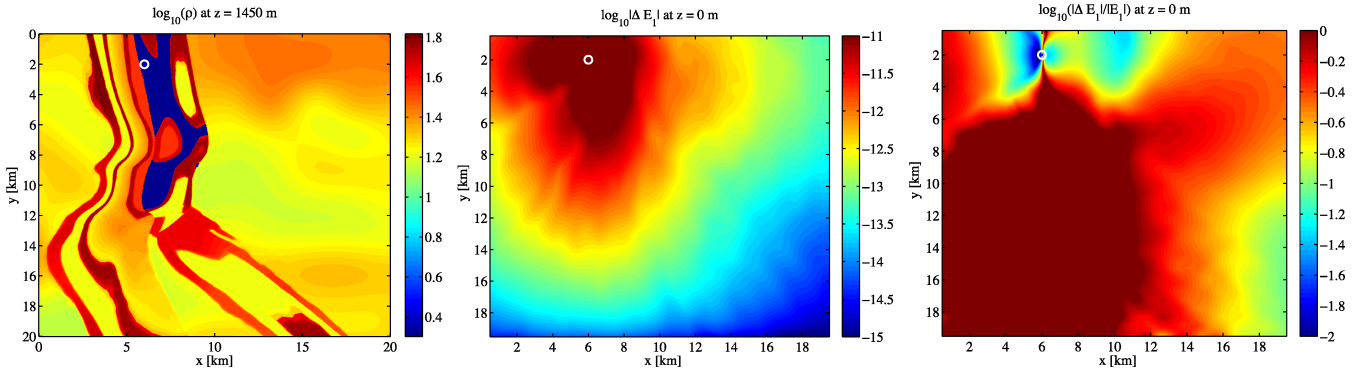

Figure 16. The left-hand panel displays a horizontal cross-section of the resistivity at reservoir depth. The centre panel shows the absolute difference of E_1, measured on the surface, for a dipole source in the z-direction at a position of (6, 2, 0.9) km. The frequency was set to 1 Hz. With the reciprocity theorem, the centre panel can also be interpreted as a result of placing a receiver in the well and placing a moveable source at a dense array of points on the surface. The white circle indicates the well location in map view. The right-hand panel shows the relative absolute difference of E_1. Because of reciprocity, the same result will be obtained for dipole sources in the x-direction at the surface and a vertical antenna that measures E_3 in the well.

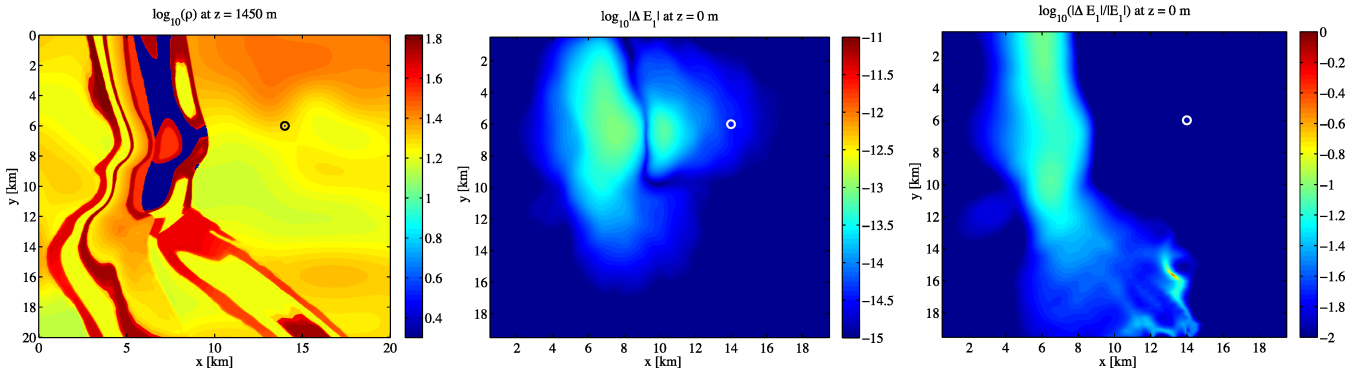

Figure 17. As Fig. 16, but with the source positioned at (14, 6, 0.9) km.

the near-surface and natural or man-made signals. In this section, we discuss the various types of 'noise' that can occur in a time-lapse experiment and describe how they can be incorporated in the numerical experiments.

6.1 Near-surface effect

One type of repeatability error in time-lapse EM data is due to changes in the near-surface environment. In time-lapse CSEM, we cannot expect the near-surface environment to be the same between surveys. Frost, for instance, will increase the resistivity of the top soil and affect the time-lapse EM measurements. Topography and near-surface inhomogeneities also plays a role and can have a strong imprint on the CSEM data as shown, for example, by Li & Constable (2007) in a marine setting. Strack (1992) refers to the distortion caused by near-surface lateral discontinuities as a static shift and suggests a correction called the calibration factor. We refer to his book for more details. Here, we present an example that illustrates the effect of near-surface changes on time-lapse EM without the correction with the calibration factor. For simplicity, we only consider a resistivity change in the top soil due to, for instance, seasonal or diurnal temperature variations. Hayley *et al.* (2007) showed an empirical approximation of 1.8–2.2 per cent change in bulk electrical resistivity per °C. In the context of agriculture and flood forecasting, the soil penetration of frost has been extensively studied, for example by Peck & O'Neill (1997) and DeGaetano *et al.* (2001). The frost penetration typically reaches a depth of the order of a metre. In dry areas, precipitation will have a strong effect. Without being specific about the cause of the near-surface variation, we increased the resistivity by 5 per cent in the grid cells just below and adjacent to the surface. These cells had a cell height of 25 m.

Fig. 18 displays the amplitude behaviour in the horizontal electric field components at 1 Hz for the same case as in Fig. 7 but with the near-surface resistivity increase included. Here the sweep efficiency is 100 per cent. The top panels of Fig. 18 show the effect of near-surface on the absolute amplitude change, whereas the bottom panels display the relative change. Although the presence of the near-surface effect produces a strong source imprint in the plots of the absolute difference, the relative changes are similar to those in Fig. 7, where the near-surface effect was absent.

Fig. 19 shows a vertical cross section of the absolute difference of E_1, E_2 and E_3 at $y = 3000$ m for the same case as in Fig. 14 but with the near-surface resistivity increase included. Again, we can see the strong source imprint appearing in all three electric components. These results demonstrate that the source should be put at some distance from the target. If it is too close, the repeatability error in the strong signal close to the source will mask the desired signals from the depleted area.

Near-surface changes will also cause a source imprint in walk-away surveys with a monitoring borehole, as shown in the Fig. 20, but the effect is relatively small and localized.

6.2 Repeatability errors

The second source of distortions in time-lapse EM data is due to incorrect amplitude measurements caused by receiver mispositioning and misalignment, improper definition of gain, receiver area, current, A/D offsets, etc. We refer to these differences as repeatability errors. In land EM surveys, the impact of these adverse effects can be reduced by better instrumentation and field procedures, as suggested by Strack (1992). We assume that these differences still produce small changes in the time-lapse EM data. In the numerical experiments presented further on, we mimicked the repeatability errors by adding random numbers to the measured electric fields with a maximum amplitude of 1 per cent relative to the signal strength at each receiver.

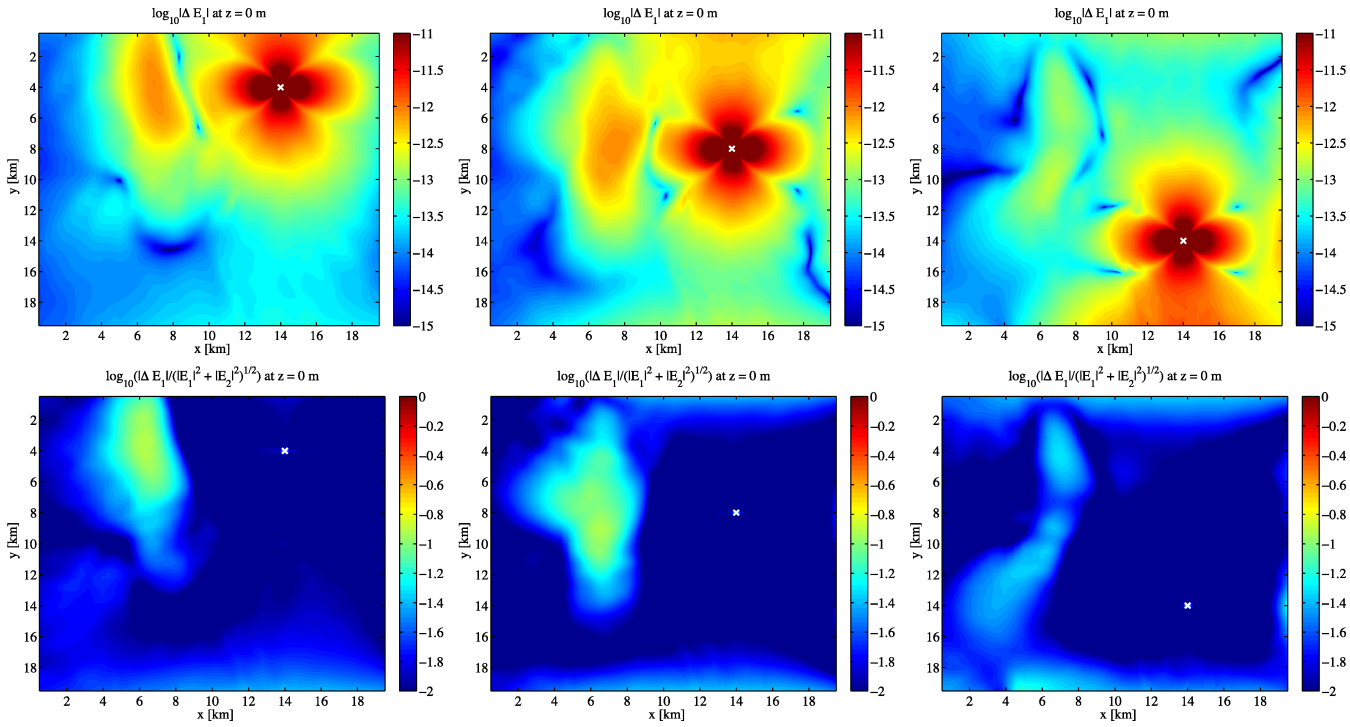

Figure 18. As Fig. 7, but with the increase of the near-surface resistivity included. This increase causes large absolute differences in the time-lapse field close to the source.

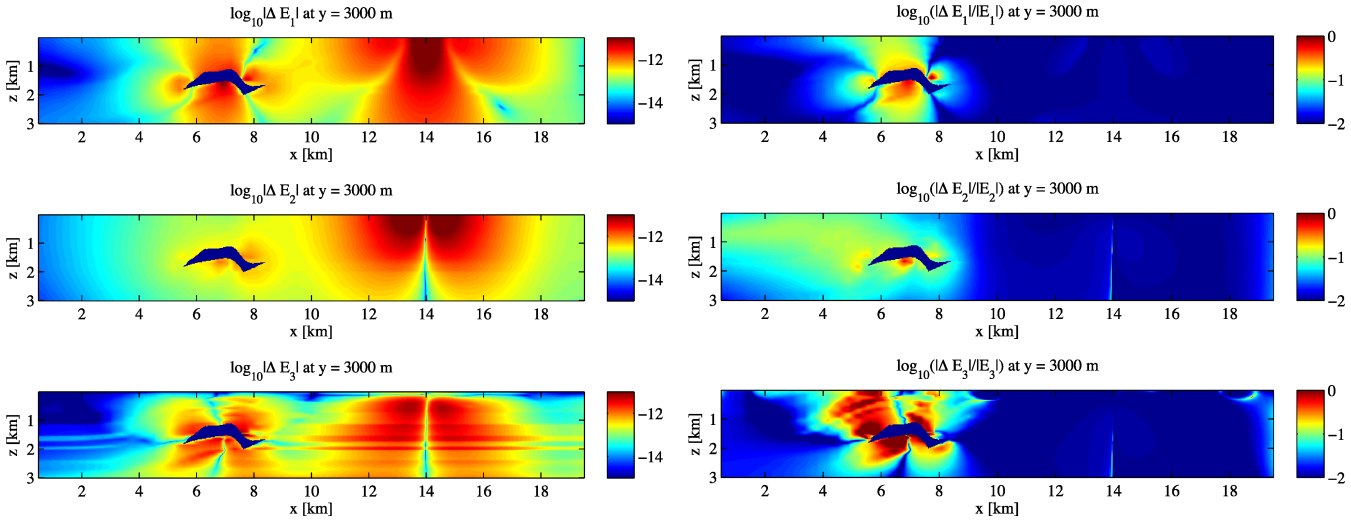

Figure 19. As Fig. 14, but with the increase of the near-surface resistivity included. Again, the effect is strongest close to the source.

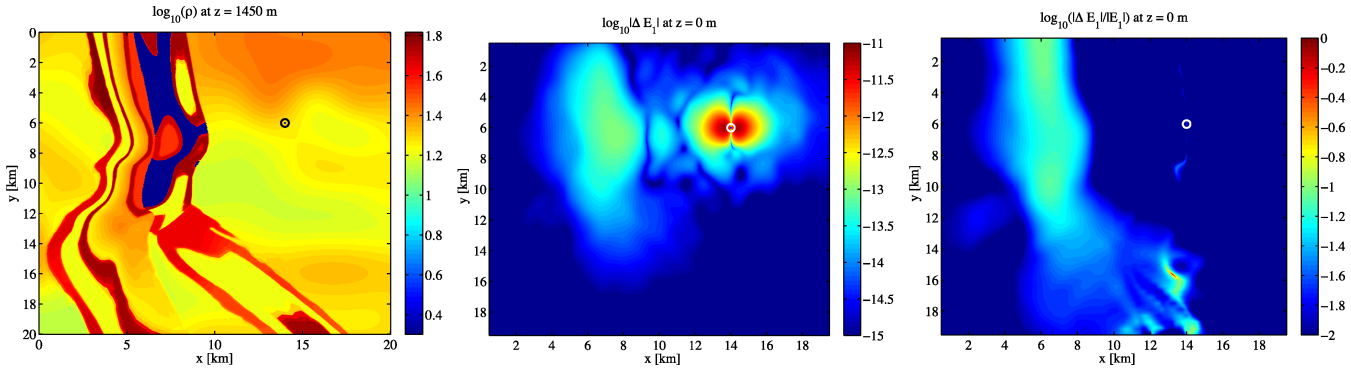

Figure 20. As Fig. 17, but for a receiver in a monitoring well and with the increase of the near-surface resistivity included.

6.3 Measurement noise

Whereas repeatability errors tend to show up as multiplicative noise, there are various additive noise sources that also affect CSEM measurements. Examples are cultural interference, natural magnetotelluric signals, and instrument noise. Obviously, these should also be taken into account in our monitoring study.

In general, noise caused by cultural interference can be classified as periodic or sporadic noise. Periodic noise is mainly generated by man-made EM sources, such as power and telephone lines. Sporadic noise is caused by current surges in the power network, motion of magnetic material near the receivers, and so on. Although this noise in practice would pollute the wanted signals, its removal is not too difficult. Strack (1992) suggests the removal of the periodic noise with digital filters and of the sporadic noise by selective stacking techniques.

The magnetotelluric background comprises EM signals caused by natural sources as thunderstorms and interactions of the solar wind with the ionosphere and magnetosphere. Between 10 kHz and 1 Hz, the MT signals are primarily caused by thunderstorms, whereas below 1 Hz they originate from magnetosphere pulsations. There is a signal gap between 0.1 and 1 Hz. The recorded signal will definitely suffer from this type of noise, but its impact can still be reduced by careful measurements and processing. One way to overcome the natural noise is by increasing the source moment to a level where the desired time-lapse signal is large enough compared to the level of the natural background noise. Reference measurements at a distance from the reservoir can also help to reduce the impact of magnetotelluric interference.

A recording instrument has a certain noise floor and a limited dynamic range. Typical values for marine applications can be found in papers by, for instance, Webb *et al.* (1985) and Flosadóttir & Constable (1996). The noise level depends on the frequency and the antenna length. For land applications, the noise floor of the sensor can be a bit higher than the one for marine. Pedersen (1988), for instance, mentions a noise floor density for the sensor of about 5×10^{-9} V $(\mathrm{m}\sqrt{\mathrm{Hz}})^{-1}$ at 1 Hz. For the electric field, this amounts to 5×10^{-9} V m^{-1} if the measurements were carried out during 1 s. Here we divided the spectral noise density by the square root of the measurement duration. Although instrumentation has improved over the last 20 yr, we nevertheless adopt Pedersen's estimate. The noise floor is quite high compared to the size of the time-lapse differences shown in Fig. 3. One way to overcome the noise is by increasing the source moment, as is also done for reducing the effect of MT signals. In the numerical experiments, we chose a noise amplitude of 10^{-11} V m^{-1}. This is relatively low compared to Pedersen's value. To have the same behaviour using Pedersen's value, that would require the source moment approximately 100 times larger than the current source moment. Note that we assumed that cultural noise and natural MT background can be removed by pre-processing of the data.

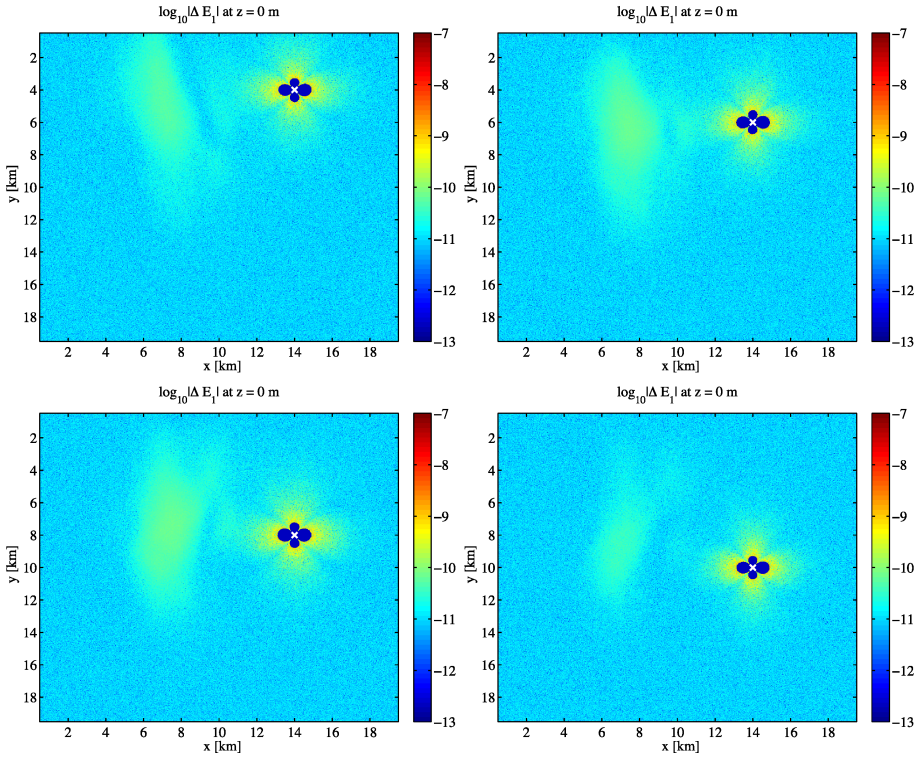

Figure 21. The time-lapse difference of the electric-field component E_1 with added noise at 1 Hz, recorded on the surface (top view) for a surface source with an x-position of 14 km and with $y = 4$, 6, 8 or 10 km, shown top-left, top-right, bottom-left- and bottom-right-hand panel, respectively. The blue four-leaf clover pattern is the result of clipping the data to the dynamic range.

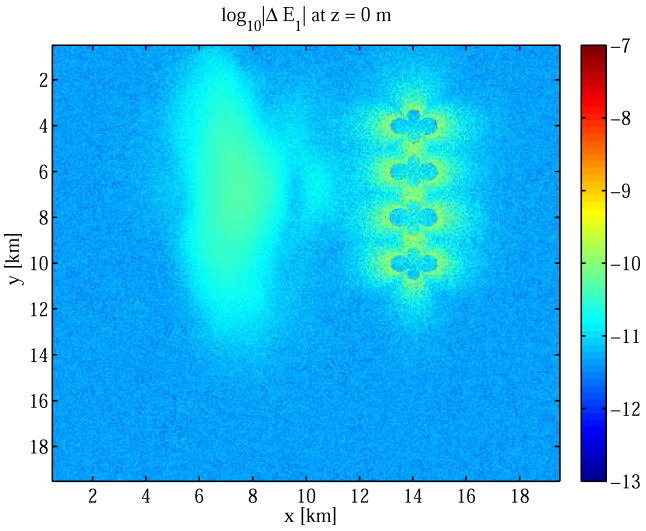

Figure 22. Average time-lapse change in E_1 after stacking data for four different source positions. Sources were located on the surface with an x-position of 14 km and with $y = 4$, 6, 8 and 10 km.

6.4 Incorporating noise into the modelling

We added the effect of various sources of noise, except the near-surface effect, to the numerical modelling results in the following way.

(i) We first calculate the electric field for the configuration that represents the resistivity model before production. We assumed a 20 A current source, as typical in land EM experiments. In the earlier experiments, we considered only the unit source.

(ii) At each receiver, we then generate a random number with a maximum amplitude of 10^{-11} V m^{-1} and add this to the recorded field.

(iii) We include the repeatability error by adding a random number with a maximum amplitude of 1 per cent relative to signal strength at each receiver.

(iv) We repeat the above three steps for the configuration that represents the resistivity model after production.

(v) We include a 6-decade dynamic range of the recording by suppressing data outside the range of 10^{-13} to 10^{-7} V m^{-1}.

Fig. 21 displays the difference in absolute amplitudes of the electric field component E_1 for various source positions. Here we applied 100 per cent sweep efficiency as used in Fig. 7. Although the noise dominates the signal, we can still observe the changes in resistivity above the reservoir.

If we take a closer look at Fig. 21, we observe that different parts of reservoir are illuminated for different source positions. This suggests stacking of the EM data for different source positions to recover the shape of the reservoir. Fig. 22 shows the average after stacking data from the four source locations displayed in Fig. 21. Although the source imprint remains, the shape of the reservoir is better defined.

7 CONCLUSIONS

We have studied the effect of resistivity changes due to oil production on land CSEM measurements for a complex geological model. We considered a surface-to-surface acquisition geometry as well as a surface-to-borehole configuration with a vertical monitoring well. The results show that the resistivity change due to displacing oil by brine can produce a small but measurable change in the CSEM response. How well the time-lapse change is confined to the

area above the resistivity change, depends on the placement of the sources and receivers. The results suggest that there are optimal distances between sources, receivers and the target area. If the source is close to the receiver and the target, the signal will be dominated by direct field and the time-lapse signal will be masked. If the distance is too large, the time-lapse signal will become too weak to be detected. This implies that the acquisition can be optimized for a given target configuration.

An alternative acquisition geometry consists of a single vertical monitoring well and sources at various surface positions. Our results for this walk-away setting suggest that the technique can be an attractive choice if the vertical electric component is measured in the well. Our study suggest that for the land example considered here, the detection of time-lapse changes due to production by time-lapse EM measurements will require a repeatability error of 1 per cent or less, as well as proper removal of interfering coherent signals.

ACKNOWLEDGMENTS

Marwan Wirianto received financial support from the sponsors of the Delphi consortium.

REFERENCES

Aminzadeh, F., Brac, J. & Kunz, T., 1997. *3-D Salt and Overthrust Models,* Society of Exploration Geophysicists, Tulsa, Oklahoma.

Archie, G.E., 1942. The electrical resistivity log as an aid in determining some reservoir characteristics, *Petrol.Trans. AIME,* **146,** 54–62.

Black, N. & Zhdanov, M.S., 2009. Monitoring of hydrocarbon reservoirs using marine CSEM method, *SEG Tech. Prog. Expanded Abstracts,* **28**(1), 850–854.

Cheesman, S.J., Edwards, R.N. & Chave, A.D., 1987. On the theory of seafloor conductivity mapping using transient electromagnetic systems, *Geophysics,* **52,** 204–217.

Cox, C.S., 1981. On the electrical conductivity of the oceanic lithosphere, *Phys. Earth planet. Inter.,* **25,** 196–201.

Cox, C.S., Constable, S.C., Chave, A.D. & Webb, S.C., 1986. Controlled source electromagnetic sounding of the oceanic lithosphere, *Nature,* **320,** 52–54.

Darnet, M., Choo, M.C.K., Plessix, R.-E., Rosenquist, M.L., Yip-Cheong, K., Sims, E. & Voon, J.W.K., 2007. Detecting hydrocarbon reservoirs from CSEM data in complex settings: application to deepwater Sabah, Malaysia, *Geophysics,* **72**(2), WA97–WA103.

de Hoop, A.T., 1995. *Handbook of Radiation and Scattering of Waves,* Academic Press, London.

DeGaetano, A.T., Cameron, M.D. & Wilks, D.S., 2001. Physical simulation of maximum seasonal soil freezing depth in the United States using routine weather observations, *J. appl. Meteorol.,* **40,** 546–555.

Eidesmo, T., Ellinsgrud, S., MacGregor, L.M., Constable, S., Sinha, M.C., Johansen, S., Kong, F.N. & Westerdahl, H., 2002. Sea Bed Logging (SBL), a new method for remote and direct identification of hydrocarbon filled layers in deepwater areas, *First Break,* **20**(3), 144–152.

Ellinsgrud, S., Eidesmo, T., Johansen, S., Sinha, M.C., MacGregor, L.M. & Constable, S., 2002. Remote sensing of hydrocarbon layers by sea bed logging (SBL): results from a cruise offshore Angola, *The Leading Edge,* **21,** 972–982.

Evans, R.L., Constable, S.C., Sinha, M.C. & Cox, C.S., 1991. Upper crustal resistivity structure of the East Pacific Rise near 13°N, *Geophys. Res. Lett.,* **18,** 1917–1920.

Flosadóttir, A.H. & Constable, S., 1996. Marine controlled-source electromagnetic sounding 1. Modeling and experimental design, *J. geophys. Res.,* **101**(B3), 5507–5517.

Griffiths, D.J., 1999. *Introduction to Electrodynamics,* Prentice Hall, Inc., Englewood Cliffs, NJ.

Gutknecht, H.H., 1993. Variants of BiCGStab for matrices with complex spectrum, *SIAM J. Scient. Stat. Comput.,* **14**(5), 1020–1033.

Hayley, K., Bentley, L.R., Gharibi, M. & Nightingale, M., 2007. Low temperature dependence of electrical resistivity: implications for near surface geophysical monitoring, *Geophys. Res. Lett.,* **34,** L18402.

He, Z., Dong, W. & Lei, Y., 2007. Joint processing and integrated interpretation of EM and seismic data—an effective method for detecting complicated reservoir targets, *The Leading Edge,* **26**(3), 336–340.

Jackson, J.D., 1999. *Classical Electrodynamics,* 3rd edn, John Wiley & Sons, Inc., New York.

Landrø, M., Veire, H.H., Duffaut, K. & Najjar, N., 2003. Discrimination beetwen pressure and fluid saturation changes from marine multicomponent time-lapse seismic data, *Geophysics,* **68**(5), 1592–1599.

Li, Y. & Constable, S., 2007. 2-D marine controlled-source electromagnetic modelling. Part 2: the effect of bathymetry, *Geophysics,* **72**(2), WA63–WA71.

Lien, M. & Mannseth, T., 2008. Sensitivity study of marine CSEM data for reservoir production monitoring, *Geophysics,* **73**(4), F151–F163.

MacGregor, L.M., Barker, N., Overton, A., Moody, S. & Bodecott, D., 2007. Derisking exploration prospects using integrated seismic and electromagnetic data—a Falkland Islands case study, *The Leading Edge,* **26**(3), 356–359.

Meju, M.A., Gallardo, L.A. & Mohamed, A.L., 2003. Evidence for correlation of electrical resistivity and seismic velocity in heterogeneous near-surface materials, *Geophys. Res. Lett.,* **30**(7), 1373–1376.

Mulder, W.A., 2006. A multigrid solver for 3-D electromagnetic diffusion, *Geophys. Prospect.,* **54**(5), 633–649.

Mulder, W.A., 2008. Geophysical modelling of 3-D electromagnetic diffusion with multigrid, *Comput. Visual. Sci.,* **11**(3), 129–138.

Mulder, W.A., Wirianto, M. & Slob, E.C., 2008. Time-domain modeling of electromagnetic diffusion with a frequency-domain code, *Geophysics,* **73**(1), F1–F8.

Orange, A., Key, K. & Constable, S., 2009. The feasibility of reservoir monitoring using time-lapse marine CSEM, *Geophysics,* **74**(2), F21–F29.

Peck, L. & O'Neill, K., 1997. Frost penetration in soil with an inclusion of sand: dependence on soil moisture content and winter severity, *Can. Geotech. J.,* **34,** 368–383.

Pedersen, L.B., 1988. Some aspects of magnetotelluric field procedures, *Surv. Geophys.,* **9,** 245–257.

Plessix, R.-E., Darnet, M. & Mulder, W.A., 2007. An approach for 3-D multisource multifrequency CSEM modeling, *Geophysics,* **72**(5), SM177–SM184.

Raiche, A.P. & Coggon, J.H., 1975. Analytic Green's tensors for integral equation modelling, *Geophysical J. Roy. astr. Soc.,* **42**(3), 1035–1038.

Strack, K.-M., 1992. *Exploration with Deep Transient Electromagnetics,* Elsevier, Amsterdam.

Strack, K.-M. & Pandey, P.B., 2007. Exploration with controlled-source electromagnetics under basalt cover in India, *The Leading Edge,* **26**(3), 360–363.

van der Vorst, H.A., 1992. Bi-CGSTAB: a fast and smoothly converging variant of Bi-CG for the solution of non-symmetric linear systems, *SIAM J. Scient. Stat. Comput.,* **13**(2), 631–644.

Vasco, D.W., Keers, H., Khazanehdari, J. & Cooke, A., 2008. Seismic imaging of reservoir flow properties: resolving water influx and reservoir permeability, *Geophysics,* **73**(1), O1–O13.

Ward, S.A. & Hohmann, G.W., 1987. Electromagnetic theory for geophysical applications, in *Electromagnetic Methods in Applied Geophysics—Theory,* Vol. 1, pp. 131–311, ed. Nabighian, M.N., Society of Exploration Geophysicists, Tulsa, Oklahoma.

Webb, S.C., Constable, S.C., Cox, C.S. & Deaton, T.K., 1985. A seafloor electric field instrument, *J. Geomagnet. Geoelectr.,* **37,** 1115–1129.

Weiland, T., 1977. A discretization method for the solution of Maxwell's equations for six-components fields, *Electron. Commun.,* **31**(3), 116–120.

Yee, K., 1966. Numerical solution of initial boundary value problems involving Maxwell's equations in isotropic media, *IEEE Trans. Antenn. Propagat.,* **16,** 302–307.